powders

MDPI

Article

Effect of YB_4 Reinforcement on the Microstructural Evolution and Mechanical Behaviour of AISI 420 Composites Produced by Vacuum Induction Melting

M. Sadhasivam [1,*], Mainak Saha [2,*], L. John Berchmans [3], S.P. Kumaresh Babu [4] and SankaraRaman Sankaranarayanan [4]

[1] School of Interdisciplinary Design and Innovation, Indian Institute of Information Technology, Design and Manufacturing, Kancheepuram, Chennai 600127, India
[2] Research Centre for Structural Materials, National Institute for Materials Science (NIMS), Sengen, Tsukuba 305-0047, Ibaraki, Japan
[3] CSIR—Central Electrochemical Research Institute (CECRI), Karaikudi 630003, India; ljberchmans@gmail.com
[4] Department of Metallurgical and Materials Engineering, National Institute of Technology, Tiruchirappalli 620015, Tamil Nadu, India; babu@nitt.edu (S.P.K.B.); raman@nitt.edu (S.S.)
* Correspondence: sadhasivam@iiitdm.ac.in (M.S.); saha.mainak@nims.go.jp (M.S.); Tel.: +81-080-3606-7062 (Mainak Saha)

Abstract

The influence of YB_4 particle addition on the microstructure and the associated thermal and mechanical properties of AISI 420 stainless steel composites fabricated using the vacuum induction melting technique was investigated. Microstructural analysis using scanning electron microscopy (SEM) confirmed the presence of YB_4 particles within the BCC-structured martensitic matrix and also along the grain boundaries across all weight fractions. In addition, YB_4 addition resulted in a pronounced refinement of the martensitic matrix, as evidenced by a progressive reduction in the size of the packets, i.e., a group of martensitic laths/plates sharing the same habit plane variants with the parent austenite grain. The presence of YB_4 particles induced internal stresses and microstrains, leading to peak shifting and broadening of the X-ray diffraction (XRD) peaks corresponding to that of the martensitic matrix phase. The coefficient of thermal expansion (CTE) decreased significantly from 13.4×10^{-6} K^{-1} for monolithic AISI 420 to 8.06×10^{-6} K^{-1} for the AISI 420/4 wt.% YB_4 composite and was attributed to the excellent dimensional stability of YB_4 particles. The maximum hardness (913.12 HV) and tensile strength (930 MPa) were achieved for the AISI 420/4 wt.% YB_4 composite. Fractographic analysis using SEM indicated a transition from ductile to brittle fracture with increasing YB_4 content, suggesting a reduction in strain-hardening capacity. The contributions of various strengthening mechanisms were quantified using the summation of strengthening and modified Clyne models, revealing that strengthening due to load bearing is dominant across all composites. Insights gained from these results are important to strategize the design of boride-based metal-matrix composites with enhanced strength–ductility synergy for structural applications.

Keywords: AISI 420; YB_4; microstructure; mechanical properties; strengthening mechanisms

Academic Editor: Paul F. Luckham

Received: 29 December 2025
Revised: 14 February 2026
Accepted: 24 February 2026
Published: 3 March 2026

1. Introduction

AISI 420 is a martensitic stainless steel (MSS) containing 12–14 wt.% chromium and up to 0.2 wt.% carbon [1]. Compared with other stainless steel grades, MSS is relatively cost-effective due to the absence of expensive alloying elements. Consequently, AISI 420 is

widely used in steam generator components, pressure vessels, pipelines, valves, cutting tools, turbines, shafts, and pump impellers in the oil and gas industry [1–5]. However, components fabricated from AISI 420 often experience severe erosion under service conditions. Its limited mechanical strength and poor wear resistance restrict its application in aggressive environments, necessitating the enhancement of its hardness, mechanical, and tribological properties [6].

In order to improve the performance of AISI 420, several approaches such as alloying addition, surface modification, heat treatment, and coating techniques have been extensively explored [1,3,5]. Dodds et al. [6] employed friction stir processing (FSP) to modify the microstructure of AISI 420 stainless steel, reporting improved hardness and superior wear resistance compared to conventionally heat-treated samples. Mirshekari et al. [1] deposited Stellite-6 coatings on AISI 420 using the gas tungsten arc welding (GTAW) process and demonstrated enhanced mechanical and wear resistance due to the formation of Stellite interlayers. Sun et al. [7] investigated the influence of in situ quenching and tempering on laser-cladded AISI 420 stainless steel powder deposited on 300 M steel substrates, observing improved ductility following in situ tempering. Nath et al. [8] examined the microstructure, corrosion behavior, and mechanical properties of additively manufactured AISI 420 in both as-printed and heat-treated conditions, reporting significant improvements in mechanical properties after heat treatment.

Metal matrix composites (MMCs) have also been widely investigated as effective materials to enhance the mechanical and tribological performance of engineering materials [9–16]. In recent years, MMCs reinforced with ceramic particles have gained considerable attention due to their superior functional and structural properties [9,10]. The uniform distribution, morphology, and interfacial bonding of reinforcement particles play a crucial role in determining the mechanical performance of MMCs. Steel-based composites reinforced with ceramic particulates have demonstrated superior physical, tribological, and mechanical properties compared to conventional steels, enabling their application across diverse engineering sectors [11].

Among various ceramic reinforcements, borides have emerged as promising candidates for MMCs owing to their high specific stiffness, excellent oxidation resistance, high hardness, and superior tribological characteristics [12–15]. Additionally, they exhibit a lower coefficient of thermal expansion than steel and possess high thermal and electrical conductivity [16]. Consequently, steel-based MMCs reinforced with borides have shown improved hardness, wear resistance, reduced thermal expansion, high elastic modulus, and good wettability with the steel matrix [17].

MMCs can be fabricated using several processing routes, including powder metallurgy, liquid metallurgy, mechanical alloying, spray deposition, friction stir processing, and infiltration. Liquid metallurgy techniques such as liquid infiltration, squeeze casting, conventional casting, and vacuum induction melting (VIM) are commonly employed for fabricating steel-based MMCs [12,16]. Among these methods, VIM offers significant advantages, including processing under a controlled and evacuated atmosphere, effective removal of entrapped gases, slag-free melting, superior surface finish, and enhanced compositional control due to efficient electromagnetic stirring. Furthermore, VIM is considered a safer and cleaner processing route compared to conventional casting techniques [12].

Several studies have reported the improvement of mechanical and tribological properties of AISI 420 through MMC approaches. Zhang et al. [3] synthesized AISI 420/VC composites using laser cladding and observed increased microhardness and erosion resistance with increasing VC content. Duraiselvam et al. [5] fabricated NiAl–Ni_3Al intermetallic composites reinforced with TiC on AISI 420 substrates via laser cladding and reported enhanced cavitation erosion resistance and hardness compared to as-received and heat-treated

materials. Liu et al. [18] investigated the densification behavior, microstructural evolution, and mechanical properties of AISI 420/TiC composites produced by selective laser melting, demonstrating that laser power and scan rate predominantly governed densification, with high energy density conditions yielding superior mechanical properties. A comprehensive review by Das et al. [19] highlighted substantial improvements in the mechanical properties of TiC-reinforced steel composites fabricated through various processing routes. Rare earth borides are suited for nuclear applications due to their high boron content and neutron absorption capability [20]. Also, they can be adopted well for high temperature and wear resistance applications [20,21].

In summary, prior studies primarily focused on improving the properties of AISI 420 stainless steel through heat treatment, surface modification, or ceramic reinforcement using additive manufacturing techniques. However, the influence of rare earth-based ceramic reinforcement addition via conventional casting or liquid metallurgy routes on the mechanical properties of AISI 420 remains largely unexplored. In this regard, YB_4 nanoparticles improve corrosion and wear behavior of many commercially available materials such as cast iron, alloy steels, light metals, Co-based alloys and zircaloy [20]. YB_4 exhibits high hardness with high bulk modulus, high melting point, and excellent thermal stability [20,21]. Among the various yttrium boride phases, YB_4 shows the best mechanical properties together with high temperature resistance [21].

Therefore, the present study aims to investigate the effect of laboratory-synthesized YB_4-particle-reinforced AISI 420 stainless steel processed through vacuum induction melting, followed by a thorough investigation of the effects of YB_4 addition on the microstructure and the associated tensile and wear properties of the composites, with particular emphasis on the associated strengthening mechanisms. Insights obtained from this study are important for designing boride-based metal-matrix composites with enhanced strength–ductility synergy for structural applications. At the end, the authors also discuss the scopes and challenges for future works in order to address the limitations of the current study.

2. Materials and Methods

2.1. Materials

In this study, AISI 420 round bars were used as the starting material and were procured from Bharat Aerospace Alloys, Mumbai, India. The nominal chemical composition of the as-received AISI 420 stainless steel is presented in Table 1. YB_4 powders with 99% purity were employed as the reinforcement material and were synthesized in-house using a metallothermic reduction method. In this process, the reactant powders Y_2O_3 and B_2O_3 were proportionally weighed according to stoichiometric calculations derived from the reaction equation, thoroughly ground, and homogeneously mixed. Calcium was subsequently introduced as the reducing agent. The reduction reaction was conducted at 950 °C under a controlled argon atmosphere. The resulting powders exhibited particle sizes in the range of 40–60 nm. The detailed synthesis procedure has been reported in our previous publications [22,23].

Table 1. Nominal chemical composition of the as-received AISI 420 stainless steel.

Element	Fe	C	Si	Mn	P	S	Cr	Ni	Mo	Co
Wt.%	Balance	0.14	0.54	0.95	0.02	0.021	13.03	0.097	0.018	0.03

2.2. Characterization of the Synthesized Powders

The morphology and size of the obtained yttrium boride powders were determined using scanning electron microscopy (SEM) and transmission electron microscopy (TEM). For SEM studies, a Zeiss Supra 40 VP microscope (Carl Zeiss AG, Oberkochen, Germany)

was used. SEM samples were prepared by dispersing 0.01 g of powder into 25 mL of ethanol, magnetically stirring for 1 h, ultrasonicating for 10 min, drop coating onto a silicon wafer using a micropipette, drying and finally, carbon coating.

Transmission electron microscopy (TEM) studies were performed using a Tecnai 20 G2 FEI microscope (EI Company, Hillsboro, OR, USA) operated at 200 kV. In the case of TEM sample preparation, all steps were similar to that of SEM sample preparation except that the powder samples were drop coated on a copper grid.

2.3. Fabrication of Composites

AISI 420/YB_4 composites were fabricated using the vacuum induction melting (VIM) technique. The as-received AISI 420 steel bars were charged into a graphite crucible and melted after evacuating the melting chamber. A high vacuum of 8×10^{-5} mbar was maintained throughout the melting process. The steel was heated to 1550 °C, after which YB_4 powder was introduced into the molten metal using a feeder mechanism connected to the vacuum chamber. The YB_4 powder was externally preheated to 300 °C under a controlled atmosphere prior to addition. The alloying (powder addition) chamber located at the top of the setup was maintained under vacuum and isolated from the melting chamber by a gate valve to prevent oxidation or contamination of the YB_4 powder during transfer. A schematic illustrating the powder feeder mechanism and the melting chamber is provided in Figure 1. Electromagnetic induction generated melt circulation, providing effective natural stirring and facilitating the uniform dispersion of YB_4 particles within the matrix. In addition to the unreinforced alloy, composites with three different reinforcement levels, 1 wt.%, 2 wt.%, and 4 wt.% YB_4, were successfully produced.

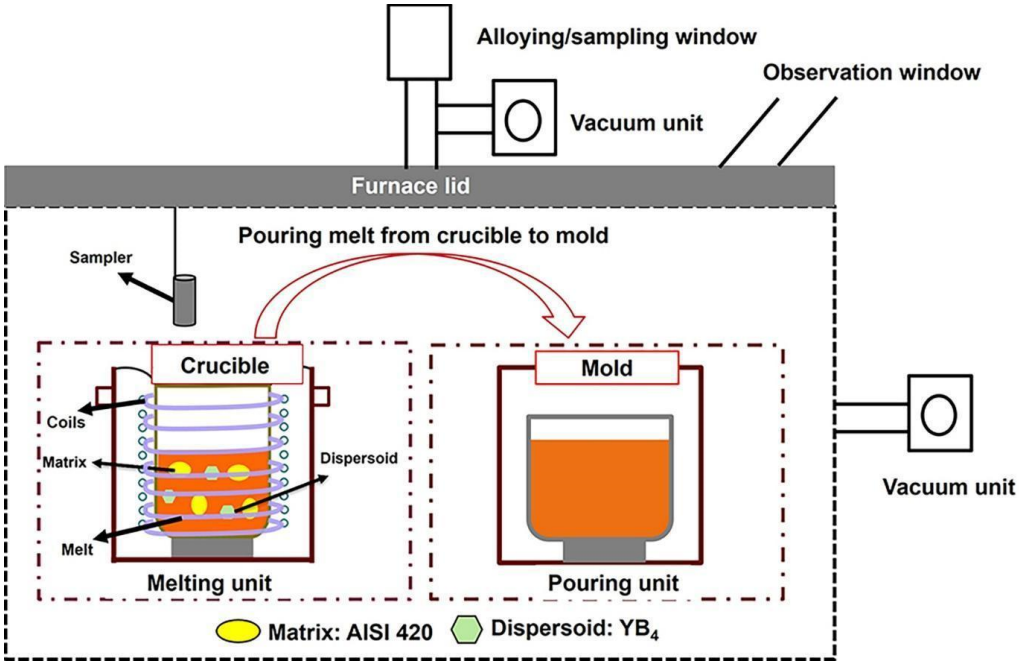

Figure 1. Schematic of the vacuum induction melting process.

2.4. Composite Characteristics

2.4.1. Density Measurements

Archimedes' principle was used to calculate the density of the fabricated AISI 420/YB_4 composites. The samples were weighed in the air followed by weighing in water medium. The weight of the samples was measured by a digital balance with 0.0001 g accuracy. By the rule of mixture, the density of the fabricated AISI 420 and its composites were calculated

theoretically as well. Porosity was determined based on the theoretical and experimental density values using formula [24]:

$$Porosity = \left(\frac{\rho_{th} - \rho_{exp}}{\rho_{th} - \rho_{air}}\right) \times 100 \quad (1)$$

where ρ_{th} refers to the theoretical density (g/cm^3) while ρ_{exp} and ρ_{air} refer to the experimental density in (g/cm^3) and density of air (0.001225 g/cm^3) respectively.

2.4.2. X-Ray Diffraction Studies

X-ray diffraction studies (XRD) were done using Rigaku Ultima III XRD (Rigaku Corporation, Tokyo, Japan) to establish the phases and their crystal structure. The samples were exposed to Cu K_α radiation (λ = 1.54056 Å) at 2°/min scanning rate. The interplanar spacing was obtained from Bragg angles and were matched with the International Centre for Diffraction data (ICDD) database values of α-iron and YB_4 phases. Note that for XRD analysis, cuboidal samples of dimensions: 1.5 × 1.5 × 1 cm^3 were metallographically polished in order to ensure flat mirror-finish surfaces, necessary for preventing any sort of distortion in peak shape and/or peak positions [25]. Considering the issue of X-ray fluorescence associated with the use of Cu K_α radiation in steels, the Ross filtering method [26] was used to obtain X-ray peaks with a high signal to noise ratio. Thin foils of Ni and Co with thicknesses of 5 μm and 5.5 μm respectively were used as filters. Two separate sets of XRD profiles were obtained, one by placing the Ni foil as a filter in front of the detector (to absorb the Cuk_β radiation) and another with Co (in order to attenuate Fe fluorescence). The X-ray peak intensities obtained from that with Co filter were subtracted from the ones obtained with Ni filter, in order to minimize the background noise and obtain a high signal to noise ratio.

2.4.3. Microstructural Studies

As-cast composite samples were examined under optical microscopy (OM, Leica DM2500 M, Wetzlar, Germany) and an SEM (model name mentioned in Section 2.2) attached to a Bruker energy dispersive spectroscopy (EDS) (Bruker Nano GmbH, Berlin, Germany) detector to analyze grain size distribution, dispersion of YB_4 particles and their morphology in matrix material respectively. EDS analysis was used to detect the elements present in the samples, except that of boron. The specimens for XRD and SEM analyses were prepared following standard metallographic procedures. Grinding was performed using SiC emery papers up to 4000 grit, followed by cloth polishing with an alumina suspension of 1 μm particle size. Final polishing was carried out using a VibroMet system (Buehler, Lake Bluff, IL, USA) with colloidal silica (particle size 0.05 μm) to obtain a deformation-free surface suitable for subsequent testing and characterization.

2.5. Microhardness Test

The hardness of the composite samples was measured by using a Matsuzawa MMT-X7B (Matsuzawa Co., Ltd., Akita, Japan) semiautomatic digital microhardness tester, which consists of a diamond indenter with a 136° phase angle. The microhardness testing was carried out on a flat and metallographically polished sample. A 300 gf indentation load was applied with 10 s dwell time. The testing was performed as per ASTM: E384-17 standards.

2.6. Coefficient of Thermal Expansion

Thermal expansion coefficient of AISI 420 and its composite samples was determined in a thermal expansion dilatometer at 5 °C/min heating rate. The thermal expansion was measured digitally with the high-resolution (1-micrometer) linear variable differential trans-

former (LVDT) measuring system. With the help of an alumina probe, the displacement of the samples (each of 10 mm initial length) was measured in the temperature range of 30–500 °C.

2.7. Tensile Test and Fracture Behavior

Tensile tests were carried out on a Tinius Olsen (H10KT) (Tinius Olsen, Horsham, PA, USA) tensile testing machine at a strain rate of 10^{-3} s^{-1} at room temperature (RT). The overall length of the samples was 100 mm with a gauge length of 25 mm, as per the ASTM E8/E8M standard for sub-size specimens. Conventional tensile properties such as yield stress (YS) at 0.2% plastic strain, ultimate tensile strength (UTS), and fracture strain were calculated for all the samples. Three samples were tested for each condition in order to ensure reproducibility and good statistics. The fracture surfaces were examined using SEM to determine the nature of the failure and the fracture mechanism.

2.8. Wear Properties

Wear tests were conducted in a DUCOM pin-on-disc wear-testing apparatus (Ducom Instruments, Bengaluru, India) under room temperature and as per the ASTM: G99 standard. Specimens with a diameter of 10 mm and a height of 15 mm were prepared for the wear study. The contact surfaces of the pins were polished up to SiC 4000-grit paper followed by cleaning with acetone. Complete contact between the samples and the disc surface was maintained. The disc material was an oil-hardened non-shrinking steel. The tests were performed at normal loads of 15 N, 30 N, 45 N and 60 N with sliding distances ranging from 750 to 1500 m, for a constant velocity of 1.2 m/s at room temperature.

3. Results and Discussions

3.1. Metallothermic-Reduced YB_4 Powders

In our earlier study, nano-sized yttrium boride powders were successfully synthesized through the metallothermic reduction route using yttria and boron oxide as reactant materials and calcium as a reductant [23]. The synthesis temperature (950 °C) was much lower than that of conventional solid-state mixing and the arc or induction melting process. Also, bulk fabrication of the product was achieved in this study.

Through XRD studies of the synthesized powder, the formation of YB_4 and YB_6 phases are confirmed, Figure 2a. Tetragonal and cubic crystal structures were determined for YB_4 and YB_6 phases respectively. The average crystallite size measured using the FWHM value through Scherrer formulae for diffraction line (211) was 47.15 nm. The SEM image in Figure 2b shows the irregular polyhedral morphology of YB_4 and YB_6 phases. The image also indicates the average size of the particle in the range of 40 nm to 60 nm (with agglomeration). The TEM-BF image in Figure 2c shows the uneven agglomerated morphology of the nano-sized yttrium boride. The particle size varies between 40 nm and 60 nm. The formation of the YB_6 phase is attributed to its favored thermodynamics and growth kinetics during the heat treatment process. The same has been extensively discussed in our research article published elsewhere [23].

It can be observed from Table 2 that the densities obtained from experiments are closer to the theoretical densities of both AISI 420 and AISI 420/YB_4 composites. Higher density values obtained from experimental results indicate that a lower volumetric level of porosity in the fabricated AISI 420 matrix material was achieved when compared to composites. The addition of the YB_4 reinforcement increases the porosity. The increase in the porosity could be due to the air envelope in YB_4 particles during feeding or due to solidification shrinkage [14,15].

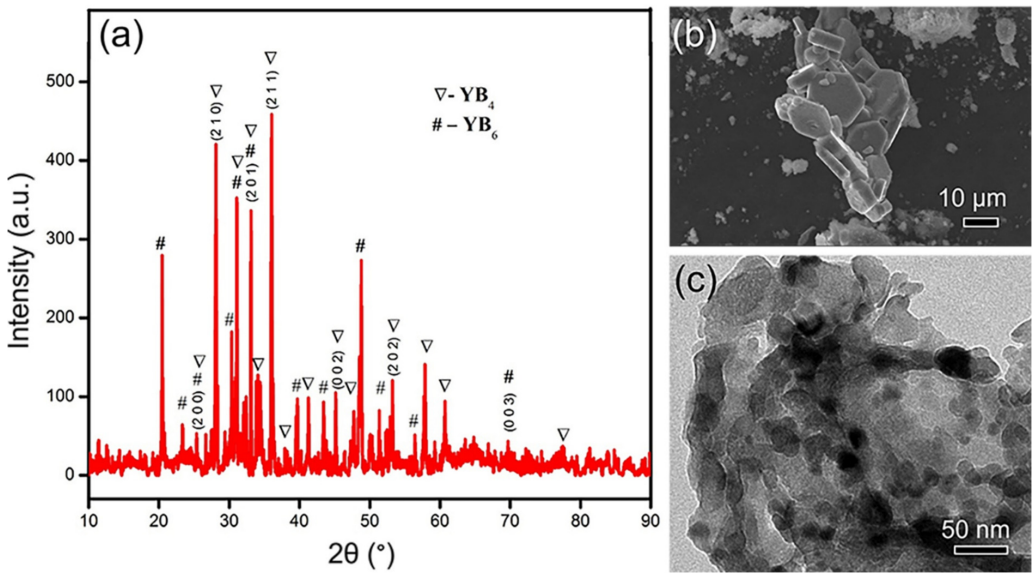

Figure 2. (**a**) X-ray diffraction (XRD), (**b**) scanning electron microscopy (SEM)—secondary electron (SE), and (**c**) transmission electron microscopy (TEM)—bright-field (BF) images of the synthesized YB_4 powders.

Table 2. Theoretical and experimental densities and porosities of AISI 420 as a function of YB_4 addition.

Material	Reinforcement (%Wt.)	Theoretical Density (g/cc)	Experimental Density (g/cc)	Porosity (Vol %)
AISI 420	0%	7.7300	7.701	0.375
AISI420/1%YB_4	1%	7.670	7.581	1.160
AISI420/2% YB_4	2%	7.612	7.483	1.695
AISI420/4% YB_4	4%	7.502	7.223	3.719

3.2. X-Ray Diffraction Studies of the Developed Composite

It can be observed in Figure 3a that the composite samples consist of martensite and YB_4 peaks. The higher intensity of YB_4 peaks corresponds to higher wt.% of the reinforcement. YB_4 peaks can be detected from 2 wt.% onwards. At 1 wt.%, the intensity of YB_4 peaks was too low to be indexed [27]. The intensity of the Fe peak decreased with addition of YB_4 particles. This structural imperfection occurred due to the addition of YB_4 and is one of the factors for the decrease in the intensity of the Fe peak. The strain involved due to the addition of YB_4 particles causes peak broadening. The peak broadening is accompanied by peak shifting due to internal stresses and induced strain [28]. The reason behind the shift of the martensite matrix peak can be due to distortion of the α-Fe lattice by YB_4 particles [28]. This causes a variation in the lattice constants, resulting in incoherent strains leading to the displacement of the matrix peak [20]. The matrix peak shift between 0% and 4% and peak broadening are shown in the inset. The existence of the YB_4 peak adjacent to the Fe matrix peak is also highlighted. The fabricated composites exhibited only the matrix and the reinforcement peaks without the presence of any other phases.

3.3. Optical Microscopy

Figure 3b presents the optical micrographs of the AISI 420/YB_4 composites. Fine YB_4 particles are observed both within the martensitic grains and along the GBs, as partly indicated using white arrows. The addition of YB_4 particles resulted in a noticeable grain refinement of the AISI 420 matrix, with the maximum refinement achieved in the composite containing 4 wt.% YB_4. This grain refinement can be attributed to YB_4 particles

which may serve as heterogeneous nucleation sites and promote the formation of finer grains [20]. Grain size analysis of the unreinforced alloy and its composites reveal a progressive reduction in the size of the martensitic packets. Note that packets refer to a group of martensitic laths/plates sharing the same habit plane variants with the parent austenite grain [29]. The packet size was determined based on the linear intercept method using ImageJ software 6.5.2 from the optical microstructure. The packet size decreased from 52 µm in the monolithic AISI 420 to 44 µm (~15.4%), 37 µm (~28%), and 29 µm (~44%) for the composites reinforced with 1, 2, and 4 wt.% YB_4, respectively. Notably, optical micrographs of composites with higher reinforcement concentration (2 and 4 wt.% YB_4) show the presence of localized agglomerations of YB_4 particles, indicated using white arrows. Such agglomeration is primarily attributed to the clustering effect, which is influenced by the solidification rate. When the solidification rate falls below the critical velocity, reinforcement particles are rejected by the advancing solidification front and accumulate at GBs, leading to segregation [30]. Nevertheless, the majority of YB_4 particles are uniformly distributed within the matrix due to the effective natural stirring induced by the vacuum induction melting process [12].

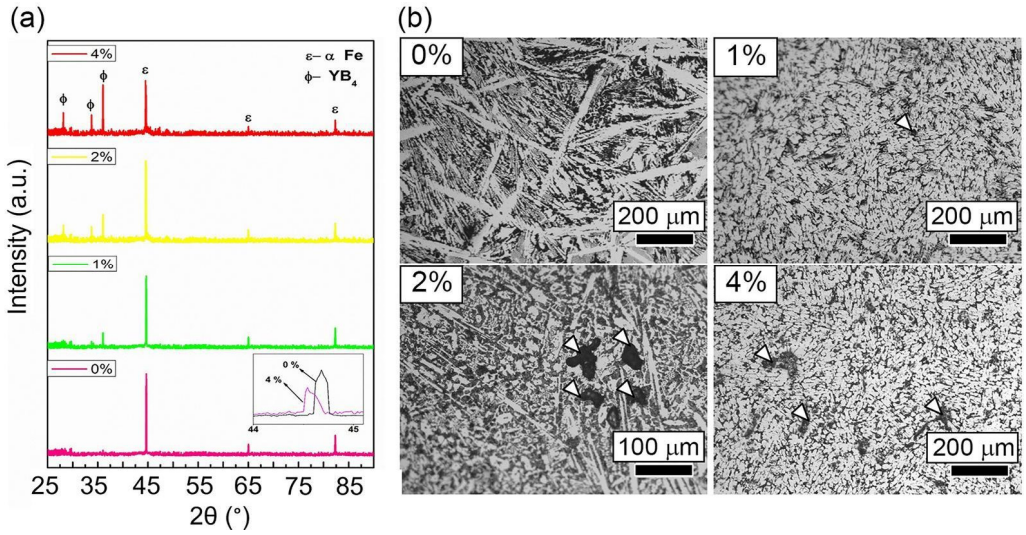

Figure 3. (**a**) XRD and (**b**) optical images of AISI 420 as a function of YB_4 addition. Note that the numbers on the upper left side of the optical images in (**b**) represent the wt.% of YB_4.

3.4. Scanning Electron Microscopy (SEM) and Energy Dispersive Spectroscopy (EDS)

The scanning electron microscopy (SEM) images shown in Figure 4 illustrate the distribution of YB_4 particles within the AISI 420 matrix. A relatively uniform dispersion of YB_4 particles (indicated using white arrows) is observed in the composite containing 1 wt.% YB_4. However, at higher reinforcement levels (2 and 4 wt.%), localized agglomeration of YB_4 particles is evident in certain regions of the matrix, as indicated using white arrows.

YB_4 particles are distributed both within the grains and along the GBs of the AISI 420 matrix, as evident from Figure 4. Fine YB_4 precipitates are observed at the grain boundary (GB) interfaces. At higher YB_4 contents (notably, 4 wt.%), evidence of GB decohesion and subsequent cracking is also observed, which is likely attributable to the significant crystallographic misfit between the martensitic matrix and the reinforced YB_4 particles. This effect is pronounced in 4 wt% YB_4-added composite due to the higher number density of YB_4 dispersoids within the martensitic matrix. Clear grain refinement with increasing YB_4 content can be observed in the microstructures. The preferential segregation of YB_4 particles at GBs results in a Zener pinning effect, wherein the particles hinder GB migration and suppress grain growth [27,30]. The pinning force becomes more effective with decreasing reinforcement particle size. Overall, grain refinement in the composites

is attributed to the combined effects of GB pinning and restricted grain growth caused by the presence of YB_4 particles, which exhibit a high nucleation rate and lead to slow grain growth kinetics. In addition, the incorporation of YB_4 particles significantly reduces the activation energy for nucleation, leading to an increased number of heterogeneous nucleation sites, which are promoted by enhanced undercooling during solidification [27].

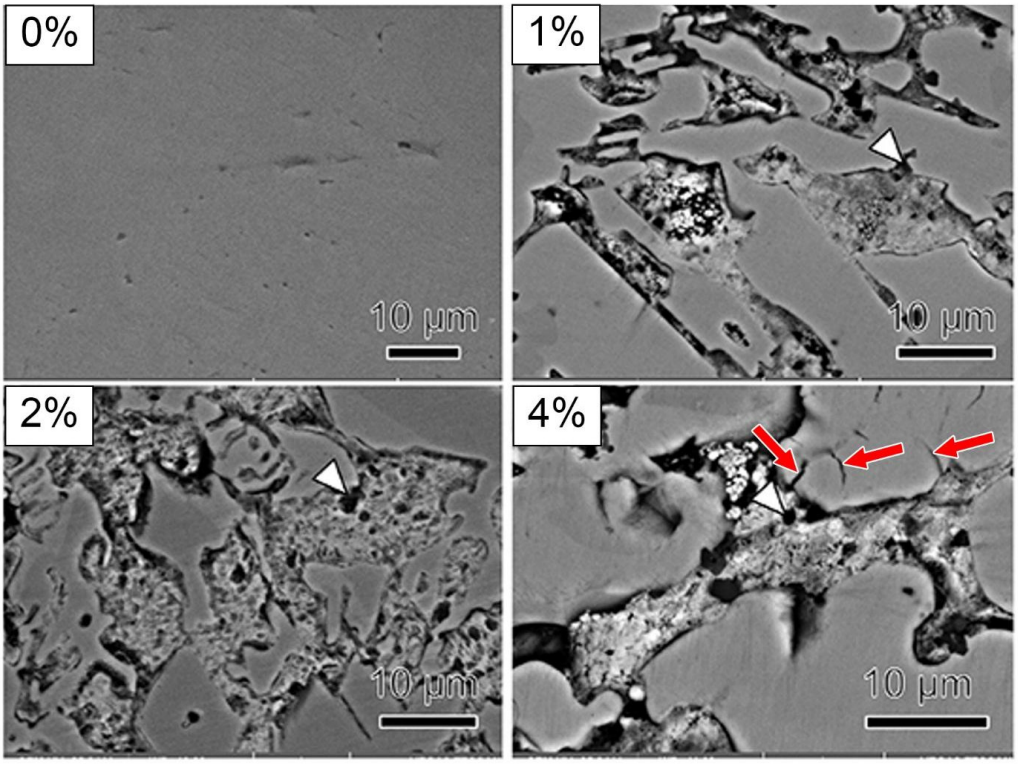

Figure 4. SEM-SE images of AISI 420 with varying YB_4 addition. YB4 particles are indicated using white arrows. Note that the numbers on the upper left of the SEM images represent the wt.% of YB_4. The parts of the cracks originating from GBs are represented using red arrows.

Energy-dispersive spectroscopy (EDS) analysis confirms the presence of yttrium, iron, and chromium in their respective atomic percentage (figure not shown). The Cr and Fe concentrations are determined as 12.5 and 87.5 at.% respectively for the composite with no YB_4 addition. On the other hand, concentrations of Cr, Y and Fe are 11.6, 0.09 and 88.31 at.% respectively for the 4 wt.% YB_4-added composite. However, the boron content could not be accurately quantified by EDS due to its low atomic number and poor fluorescence yield.

3.5. Microhardness

Figure 5a presents the microhardness results of the fabricated AISI 420/YB_4 composites. The monolithic as-cast AISI 420 exhibited the lowest hardness value of 589.5 HV. With the incorporation of YB_4 particles, a significant increase in hardness was observed, which can be attributed to the uniform dispersion of the inherently hard YB_4 reinforcement within the relatively softer steel matrix. The addition of YB_4 particles also promoted grain refinement, further contributing to the enhanced hardness of the composites. The hardness increased progressively with increasing reinforcement content, demonstrating a strong dependence on YB_4 concentration. The AISI 420/4 wt.% YB_4 composite exhibited an approximately 55% increase in hardness, reaching a value of 913.2 HV. This improvement is primarily attributed to the effective load transfer from the matrix to the reinforcement, facilitated by strong interfacial bonding between YB_4 particles and the AISI 420 matrix. Moreover, the significantly higher hardness and stiffness of YB_4 particles relative to the matrix leads to an increase in the overall hardness of the composite [31].

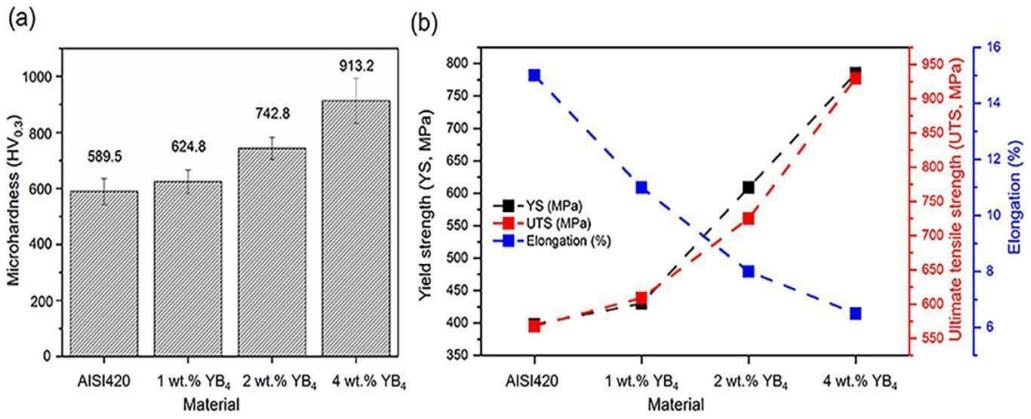

Figure 5. (**a**) Vickers microhardness with an applied load of 0.3 kgf and (**b**) tensile properties, including yield strength and ultimate tensile strength, and total elongation of AISI 420 with varying YB_4 additions. Note that the tensile tests are repeated thrice to ensure reproducibility of the mechanical properties.

3.6. Tensile Properties

The tensile properties determined at RT for AISI 420/YB_4 composite are shown as a function of YB_4 addition in Figure 5b. With the increase in YB_4 content, UTS and YS of the composite increased significantly. UTS increased by 7.2% (609.5 MPa), 28% (725.3 MPa) and 63% (930 MPa) in AISI 420/1% YB_4, AISI 420/2% YB_4 and AISI 420/4% YB_4 composites respectively when compared to the AISI 420 matrix (568 MPa). Similarly, YS improved by 8% (430.76 MPa), 54% (609 MPa), and 97% (785 MPa) in AISI 420/1% YB_4, AISI 420/2% YB_4 and AISI 420/4% YB_4 respectively compared to that of AISI 420 (398 MPa). A decrease in ductility was observed with the addition of YB_4 due to its hard and non-deformable nature. The primary reason for the improved tensile properties of the YB_4-added composite is good interfacial bonding between the matrix and the reinforcement particles.

3.7. Fractography

Figure 6 presents the tensile fracture surfaces of monolithic AISI 420 and AISI 420/YB_4 composites tested at room temperature. The fracture surface of the unreinforced AISI 420 alloy (Figure 6a) is characterized by the presence of large and deep dimples, indicating extensive plastic deformation prior to fracture and a predominantly ductile failure mode. Fracture in this alloy occurs through the nucleation, growth, and coalescence of micro-voids once they attain a critical size [31]. The presence of continuous striations on the fracture surface further suggests unhindered dislocation motion, which contributes to the enhanced ductility of the base alloy [32].

In contrast, the fracture behavior of the composites is significantly influenced by the presence of YB_4 reinforcement particles, which impede dislocation motion and thereby reduce the extent of plastic deformation. The fracture surface of the composite containing higher YB_4 content (Figure 6b) exhibits smaller dimples compared to the monolithic alloy, indicating a mixed mode of ductile–brittle fracture. With increasing YB_4 content, distinct cracks become evident on the fracture surfaces (Figure 6c), signifying a transition towards brittle fracture behavior. The presence of shallow dimples in these composites suggests a substantial reduction in strain-hardening capacity. The area fraction of dimples was qualitatively estimated using the color-thresholding method in ImageJ software. The measured dimple area fraction was approximately 59.68% for the base alloy and 32.69% for the 4 wt.% YB_4-reinforced composite. This substantial reduction in the dimple area fraction further indicates a clear transition from a ductile to a more brittle mode of fracture with reinforcement addition.

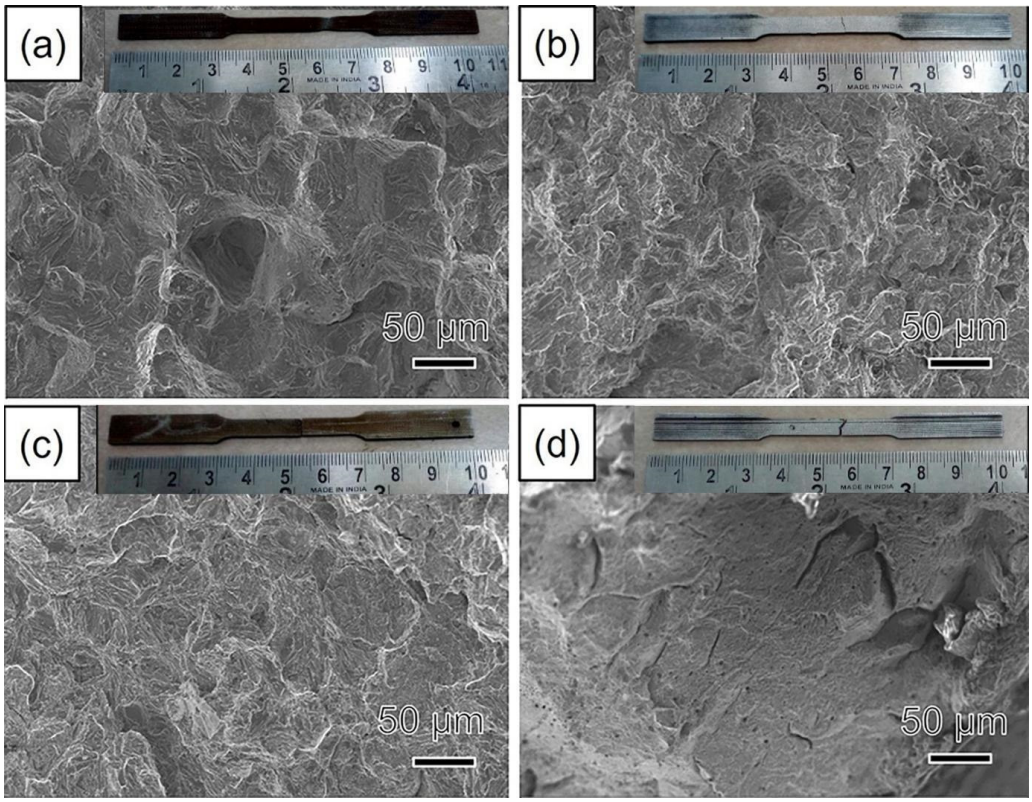

Figure 6. SEM fractographic images of AISI 420 with (**a**) 0, (**b**) 1, (**c**) 2, and (**d**) 4 wt.% YB_4. Inset images show the macrographs of tensile specimens after failure.

At the highest reinforcement level (Figure 6d), the fracture surface reveals extensive cracking with very few dimples, confirming a predominantly brittle mode of failure and a further reduction in ductility. Crack initiation is primarily attributed to stress concentration at the matrix–reinforcement interfaces caused by the presence of rigid YB_4 particles. The observed increase in the strength and concurrent decrease in the elongation of the AISI 420/YB_4 composites can be attributed to grain refinement and efficient load transfer from the matrix to the reinforcement [21,22]. During tensile loading, voids nucleate around the reinforcement particles, and dislocation motion is effectively hindered by YB_4, necessitating higher applied stresses for deformation. Final failure occurs through the growth and coalescence of these microvoids.

Macrographs of the fractured tensile specimens further corroborate these observations. The AISI 420/4 wt.% YB_4 composite exhibits no visible yielding and undergoes sudden brittle fracture, whereas the monolithic AISI 420 specimen shows fracture at the gauge center accompanied by noticeable elongation. The increasing brittleness of the composites is also reflected in the percentage elongation values, which decrease progressively with increasing YB_4 content (Figure 5b).

3.8. Analysis of Various Strengthening Mechanisms

The tensile properties, particularly the strength of YB_4-added composites, are enhanced because of various strengthening mechanisms. The improvement in the tensile properties of the composite can be attributed mainly to various strengthening mechanisms, namely, (a) grain refinement, (b) dispersion strengthening, (c) forest strengthening and (d) load bearing. In order to evaluate the contribution of different strengthening mechanisms, the prediction of YS is performed for each strengthening mechanism based on the suggested theoretical models [33]. The calculated value of total yield strength enables the prediction of the effect of the different strengthening mechanisms. The role of the

individual strengthening mechanism on the tensile property of the composites is discussed below in detail.

3.8.1. Orowan Strengthening

Orowan/dispersion strengthening is achieved when the dislocation motion is hindered by the reinforcement particle. When the dislocation motion is hindered, the dislocation either cuts through the particles or bows around the particle [34]. When the slip plane is continuous from the matrix along with the reinforcement particle then the dislocation cuts through the particle. When there is an interface in orientation then the dislocation bows across the particle [34]. The degree of strengthening from the presence of YB_4 particles depends on its size and distribution in the AISI 420 matrix. Strengthening occurs once the critical interspacing of particles is achieved. The smaller the particles, the smaller the interparticulate spacing. On the other hand, the larger the particles, the greater the distances over which they will be distributed. It requires comparatively lower stress to move the dislocation by cutting through the particle, unlike the case where the dislocation bows around the reinforcement particle, resulting in the formation of Orowan loops [34–36]. Orowan loops induce more strain on the moving dislocation resulting in a higher magnitude of force required to move the same. Effective strengthening is therefore achieved in the bowing process. The stress required to bow a dislocation is inversely proportional to the average interspacing of the particles [34–36]. Orowan strengthening is estimated using the following relation [34,36]:

$$\sigma_{Orowan} = M \cdot \frac{0.4 \cdot G \cdot b}{\pi \underline{\lambda}} \cdot \frac{\left(\frac{d}{b}\right)}{\sqrt{1-\nu_{SS}}} \tag{2}$$

$$\underline{\lambda} = 1.23r\sqrt{\frac{2\pi}{3f}}, \quad r = \frac{d}{2}, \underline{d} = \sqrt{\frac{2}{3}} \cdot d$$

where M is the mean orientation factor or Taylor factor (M = 3 for AISI 420) [36,37], G is the shear modulus of AISI 420 (75 GPa) [38], b is the burgers vector of AISI 420 (2.5×10^{-10} m) [38], d is the average particle size of YB_4 reinforcement (10^{-5} m), ν_{SS} is the poisson ratio of AISI 420 (ν_{SS} = 0.28) [36], f is the volume fraction addition of YB_4 reinforcement. The contribution of Orowan strengthening σ_{Orowan} can be calculated theoretically using Equation (2). The obtained Orowan strengths for AISI 420/1% YB_4, AISI 420/2% YB_4, and AISI 420/4% YB_4 were estimated as 13.376 MPa, 18.79 MPa, and 26.4 MPa respectively. Table 3 shows the comparison theoretically predicted and experimentally observed interparticulate spacing values along with the respective Orowan strength. Experimental interparticulate spacing values were obtained by measuring the distance between the two YB_4 particles from the SEM image, as shown in Figure 3.

Table 3. Interparticulate spacing determined both experimentally and theoretically and Orowan strengthening in AISI410 as a function of YB_4 addition.

Material	Interparticulate Spacing $\lambda_{Theoretical}$ (m)	Interparticulate Spacing $\lambda_{Observed}$ (m)	σ_{Orowan} (MPa) Theoretical	σ_{Orowan} (MPa) Observed
AISI420/1%YB_4	6.57×10^{-6}	5.46×10^{-6}	13.376	16.07
AISI420/2%YB_4	4.67×10^{-6}	3.59×10^{-6}	18.79	24.66
AISI420/4%YB_4	3.32×10^{-6}	1.57×10^{-6}	26.4	55.90

3.8.2. Strengthening by Grain Refinement

Strengthening due to grain refinement is based on the Hall–Petch theory, where the strength of the material is inversely proportional to grain size. The reason behind the effective strengthening due to reduction in grain size can be explained by the phenomenon of dislocation pile-up at GBs. Smaller grain size helps the frequent pile-up of dislocations. These dislocations pile up at the GBs and lead to increase in the yield strength of the material [38]. Strengthening due to grain refinement is determined using the following relation [34,37,38]:

$$\sigma_{Hall-Petch} = KD^{-0.5} \quad (3)$$

where K is the Hall–Petch coefficient of AISI 420 (K = 515 MPa $\mu m^{1/2}$) [38,39], D is the average grain size of microcomposites (in μm). $\sigma_{Hall-Petch}$ for AISI 420/1% YB_4 is estimated as 80.398 MPa. The Hall–Petch strength for AISI 420/2% YB_4 and AISI 420/4% YB_4 is 88.05 MPa and 108.95 MPa respectively. From these results, it is evident that the reduction in the grain size of the composite leads to the enhancement of strength.

3.8.3. Strengthening Due to Load Bearing

Strengthening due to load bearing is achieved when the applied load gets transferred from the matrix to YB_4 reinforcement effectively. The extent of strengthening due to load bearing mainly depends on the amount of the reinforcement present in the matrix and is estimated from the following shear–lag strengthening relation [34,35]:

$$\sigma_{LT} = \sigma_{ss}[1 + V_r(\frac{E_r}{E_m} - 1)] \quad (4)$$

where V_r is the volume fraction of YB_4 reinforcement, σ_{ss} is the experimental yield strength of pure as-cast AISI 420 alloy (345 MPa), E_m is the Young's modulus of AISI 420 (200 GPa) [40,41], E_r is the Young's modulus of YB4 (480 GPa) [21]. σ_{LT} for AISI 420/1% YB_4 was obtained as 353.32 MPa. For AISI 420/2% YB_4, the theoretical yield strength value was obtained as 361.98 MPa. The strength increased to 376.69 MPa for AISI 420/4% YB_4. It can be observed that σ_{LT} increased with greater addition of YB_4 reinforcements.

3.8.4. Forest Hardening

This thermal mismatch between matrix and reinforcement develops stress in the composite and, subsequently, generation of a dislocation forest near the matrix/reinforcement interface, which further contributes to the strengthening of the composite [34]. Strengthening due to dislocation forests can be estimated theoretically by the following relation [34,40]:

$$\sigma_{CTE} = A \cdot M \cdot G \cdot b \cdot {\rho_{th}}^{0.5} \quad (5)$$

$$\rho_{th} = \frac{12\sqrt{2} \cdot \Delta\alpha \cdot \Delta T \cdot f}{b \cdot d \cdot (1 - f)}$$

where A is a constant of the forest dislocation hardening in AISI 420 (=0.38) [42], M is the mean orientation factor or Taylor factor for AISI 420 (=3) [40–43], G is the shear modulus of AISI 420 (=75 GPa) [34,38], ρ_{th} is the dislocation density, b is the burgers vector of AISI 420 (=2.5 × 10^{-10} m) [43], $\Delta\alpha$ is the difference in the CTE values between the matrix and reinforcement, ΔT is the temperature deviation, ~250 K, for all the composites [35], d is the average particle size of reinforcement, f is the volume fraction of reinforcement. σ_{CTE} for AISI 420/1% YB_4 is 71.298 MPa. It is increased to 73.190 MPa and 78.529 MPa for AISI 420/2% YB_4 and AISI 420/4% YB_4 respectively.

For the theoretical prediction of the tensile YS of metal matrix composites, several models have been used in the previous studies [34]. Important strengthening models such as the

summation of strengthening model [33,36,39] and modified Clyne model [33,36,39] have been applied in our present study. In the former, the contribution of each strengthening mechanism is added along with the experimental yield strength (σ_{SS}) of the AISI 420 composite to obtain the overall strength of the composite, with the assumption that each strengthening mechanism behaves independently [36]. The summation of different strengthening can be expressed using the following relation [36]:

$$\sigma_{summation} = \sigma_{SS} + \sigma_{Orowan} + \sigma_{Hall-Petch} + \sigma_{CTE} + \sigma_{LT} \quad (6)$$

The modified Clyne model yields the net contribution of each strengthening mechanism by the square root of the sum of squares method. The square root of the sum of squares value is added to the tensile yield strength obtained experimentally for the AISI 420 alloy. Using this model, theoretical yield strength is calculated as [36]:

$$\sigma_{modifiedClyne} = \sigma_{SS} + \Delta\sigma \quad (7)$$

$$\Delta\sigma = \sqrt{{\sigma_{Orowan}}^2 + {\sigma_{Hall-Petch}}^2 + {\sigma_{CTE}}^2 + {\sigma_{LT}}^2}$$

The theoretical yield strength values obtained from various strengthening models are compared with the experimentally observed yield strength values and are shown as a function of YB_4 addition in Figure 7. Figure 7a–c corresponds to 1, 2, and 4 wt.% YB_4 additions, respectively. Even though the overall calculated yield strength is significantly higher than the experimental yield strength values, the contribution of individual strengthening mechanisms can be obtained through theoretical calculations. The yield strength values calculated theoretically for individual strengthening mechanisms after the addition of YB_4 are shown in Table 4. It may be observed that the contribution of load-bearing strengthening is the highest, with a contribution of 81.68% for the AISI 420/4 wt.% YB_4 composite. This is due to the high hardness of the YB_4 particles and good interfacial bonding between the matrix and reinforcement [31]. This is followed by grain refinement, or Hall–Petch strengthening, which contributes 9.32% of the cumulative strength. It is evident that the presence of YB_4 particles assists in heterogeneous nucleation, which leads to grain size reduction in the composites. Additionally, the presence of YB_4 at the GBs causes a Zener pinning effect, which further promotes grain refinement [24,44,45]. The contribution of dislocation strengthening accounts for 6.72% and arises from the thermal mismatch between the matrix and reinforcement [45]. Dispersion, or Orowan, strengthening contributes the least according to theoretical modelling, with only 2.26% for the AISI 420/4 wt.% YB_4 composite. This is because effective dislocation bowing occurs only when the reinforcement particle size is in the nanoscale range, resulting in smaller interparticle spacing and more effective strengthening [33,46].

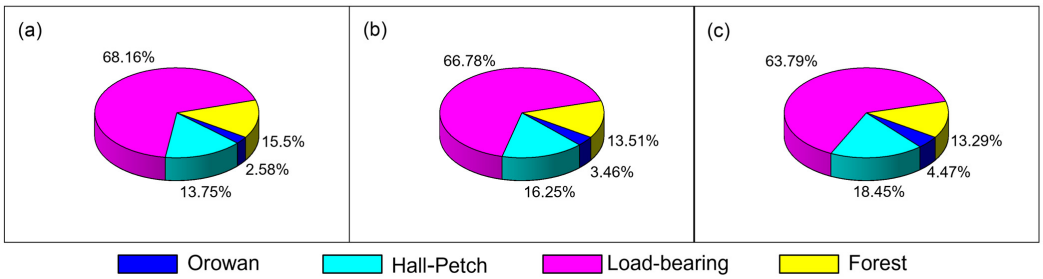

Figure 7. Strengthening contributions estimated using summation model in AISI 420 with (**a**) 1, (**b**) 2 and (**c**) 4 wt.% YB_4.

Table 4. Strengthening contributions in AISI 420 with varying YB_4 additions estimated using both summation and modified Clyne models. Note that the abbreviations CTE, LT and mod Clyne refer to coefficient of thermal expansion, load-transfer and modified Clyne respectively.

Material	YS_{exp} (MPa)	σ_{Orowan} (MPa)	$\sigma_{Hall-Petch}$ (MPa)	σ_{CTE} (MPa)	σ_{LT} (MPa)	$\sigma_{summation}$ (MPa)	$\sigma_{modClyne}$ (MPa)
AISI 420	398 ± 8	-	-	-	-	-	-
AISI420/1% YB_4	430 ± 8.5	13.376	80.398	71.298	353.32	916.39	767.54
AISI420/2% YB_4	609 ± 9	18.79	88.05	73.190	361.98	940.01	778.12
AISI420/4% YB_4	785 ± 10.5	26.4	108.95	78.529	376.69	988.57	798.79

3.9. Coefficient of Thermal Expansion

A significant reduction in the coefficient of thermal expansion (CTE) was observed with the incorporation of YB_4 particles, with the AISI 420/4 wt.% YB_4 composite exhibiting the lowest CTE value of 9.6×10^{-6} K^{-1}, compared to 13.4×10^{-6} K^{-1} for the monolithic AISI 420 alloy, as shown in Figure 8. This reduction is primarily attributed to the inherently low CTE of YB_4 (7.9×10^{-6} K^{-1}) [23]. In addition, strong interfacial bonding between the matrix and the reinforcement contributes to the effective constraint of thermal expansion in the composite. The CTE results presented in Figure 9 demonstrate that the addition of YB_4 significantly enhances the dimensional stability of the AISI 420 matrix, leading to a progressive decrease in CTE with increasing reinforcement content [24,47]. This behavior arises from the ability of YB_4 particles to restrain matrix expansion due to their low thermal expansion coefficient [47].

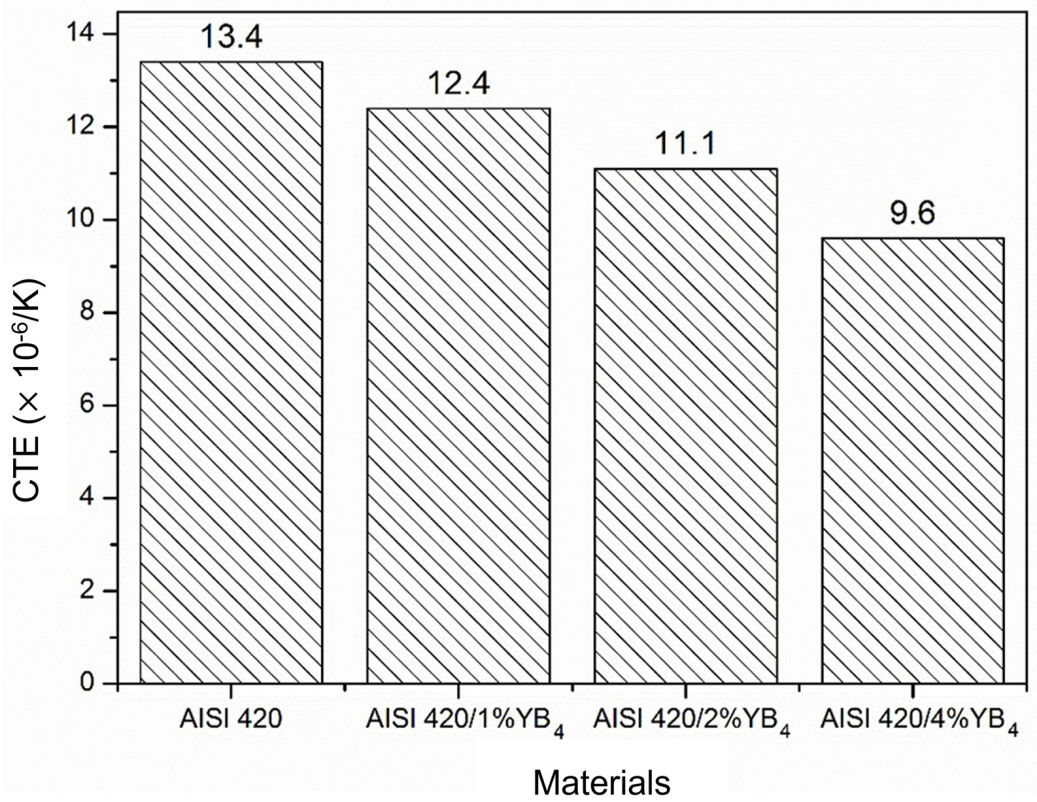

Figure 8. Coefficient of thermal expansion of AISI 420 with variation in YB_4 addition.

3.10. Wear Property of the Composites

Wear rate increased with increasing sliding distance and with the increase in applied load for all compositions. With an increase in applied loads, there was an increase in the volumetric wear rate of the materials. Wear rate decreased with an increase in wt.%

of YB_4 particles for a given load and sliding distance, as evident from Figure 9. The wear rate observed in the composites reinforced with YB_4 was less than the unreinforced alloy for all applied loads and at all operating conditions. A similar trend of improved wear resistance with increasing proportion of grain refinement was observed in previous reports [48,49]. The wear rate of pure AISI 420 at 15N load for 1500 m sliding distance was 15.889 × 10^{-5} mm^3/m (Figure 9a). The wear rate at the same dry sliding condition for AISI 420/1% YB_4, AISI 420/2% YB_4 and AISI 420/4% YB_4 were 13.973 × 10^{-5} mm^3/m, 12.840 × 10^{-5} mm^3/m and 11.161 × 10^{-5} mm^3/m respectively (Figure 9b–d).

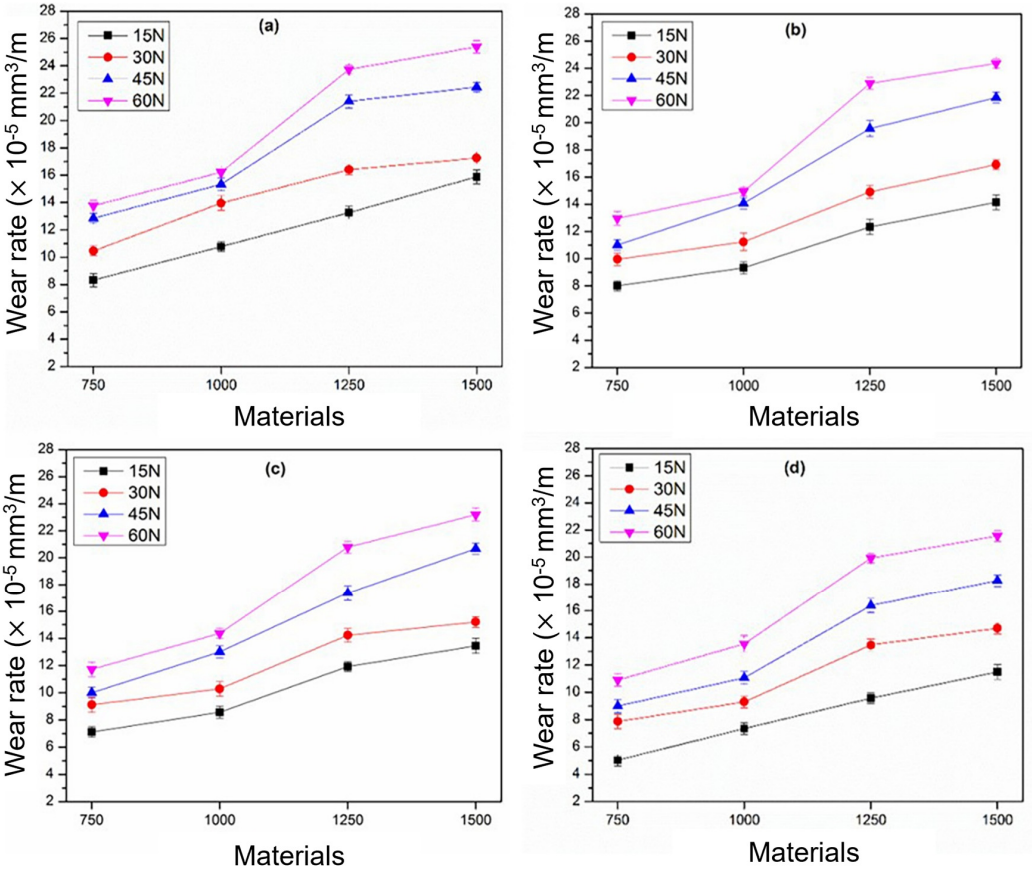

Figure 9. Wear rate vs. sliding distance estimated based on pin-on-disc experiment for AISI 420 with addition of (**a**) 0, (**b**) 1, (**c**) 2, and (**d**) 4 wt.% YB_4.

4. Conclusions

In this study, AISI 420/YB_4 composites were synthesized using the vacuum induction melting technique. The fabricated composite was subjected to microstructural characterization, and mechanical and thermal property evaluation. Some of the major conclusions that can be drawn from the results are as follows:

- XRD showed the presence of the YB_4 phase in the composites. Also, it revealed the shifting and broadening of α-Fe peaks due to internal stresses and strain induced by the YB_4 particles.
- Microstructural characterization using SEM revealed the dispersion of YB_4 particles in the matrix. It also observed that YB_4 particles act as a grain refiner by promoting heterogeneous nucleation. Grain refinement of ~44% was achieved for AISI 420/4%YB_4 when compared to the AISI 420 matrix.
- The microhardness values of the composite were enhanced with an increase in the YB_4 wt.%, with AISI 420/4%YB_4 composite showing the maximum hardness of 913 HV.

The higher hardness and stiffness of YB_4 particles led to an improvement in the hardness values of composites.

- Thermal expansion results showed a considerable decrease in the CTE value of the composite when compared to the AISI 420, with 8.06×10^{-6}/K in AISI 420/4%YB_4 compared to 13.8×10^{-6}/K in AISI 420. An increase in the dimensional stability due to the addition of YB_4 is the primary reason for the lower CTE values in the composites.
- Tensile properties of the composite indicate significant improvement in both UTS and YS values with the addition of YB_4. AISI 420/4%YB_4 exhibited superior tensile properties with the UTS of 706 MPa, ~50% higher than that of the monolithic AISI 420 alloy. Fractography analysis using SEM indicates the transition of fracture from ductile to brittle mode with the increase in the weight fraction of YB_4 particles.
- Among various strengthening mechanisms, strengthening due to load bearing has a greater influence on the overall strength of the YB_4-added composites (81.68%) followed by Hall–Petch strengthening (9.32%), forest strengthening (6.72%) and Orowan strengthening (2.26%).

5. Scopes and Challenges for Future Works

The present study indicated that the addition of YB_4 to AISI 420 stainless steel with a BCC martensitic microstructure leads to formation of dispersoids, namely YB_4 and YB_6 at GBs (Figure 4), and reinforces the composites primarily through a load-bearing mechanism (Figure 7). Here, it is important to examine the role of the structure of GBs [50–54] in the formation of dispersoids and also to examine the nature of the interface between the dispersoids and the BCC martensitic matrix. Considering the coarse size and the hard and non-shearable nature of these particles [55–58], we have hypothesized a possibility of Orowan looping around these particles. However, in-depth microstructural characterization, primarily, involving transmission electron microscopy (TEM) is required to clearly visualize the arrangement of dislocations at these interfaces [59] and will be performed in future investigations.

Also, another important point to consider is to be able to determine the concentration of boron in order to clearly distinguish between the YB_4 and YB_6. Although the present study shows the presence of elements such as Fe, Cr and Y in 4 wt.% YB_4 (Figure 4), mapping the presence of boron is highly challenging using EDS, as briefly highlighted in Section 3.4. A common method to map light elements (e.g., boron) with the highest possible spatial resolution is to use a 3D atom probe (3DAP) [60–62]. A number of studies have used 3DAP to successfully map boron [63,64] in boride-containing composites. Utilizing 3DAP to map the borides at GBs is another avenue which needs to be investigated. Regarding the possibility of correlating the structure of GBs and dislocation arrangement with near-atomic scale chemistry in their near vicinity, one of the methods that may be utilized is to perform correlative microscopy investigations across multiple length scales using techniques such as electron backscatter diffraction (EBSD), transmission Kikuchi diffraction (TKD), TEM and 3DAP. However, performing correlative microscopic characterization is largely associated with complex sample preparation procedures, especially considering the brittle nature of the reinforcement particles and dedicated instrumentation which, in most cases, is not economically viable [52,65,66]. Nevertheless, while the use of the aforementioned characterization techniques may be helpful to address some of the fundamental problems and limitations of the current study, optimization of sample preparation conditions is a vital and highly challenging part and should be treated as a pre-requisite prior to performing high-end characterization. In addition, considering that the tensile strength of the composites increases with YB_4 addition with significant reduction in ductility, an in-depth evaluation of the fatigue properties, both high-and low-cycle, with systematic microstructural correlation

is also important and is a part of an on-going investigation. Results from such a study are important to provide a basic understanding of tailoring strength–ductility synergy as a function of YB_4 reinforcement addition in AISI 420, which, in turn, would be crucial for expanding its industrial applications.

Author Contributions: M.S. (M. Sadhasivam)—conceptualization, investigation, original draft, editing and review, M.S. (Mainak Saha)—editing and review, L.J.B.—review and editing, S.P.K.B.—review, editing and resources, S.S.—review, editing, funding acquisition and resources. All authors have read and agreed to the published version of the manuscript.

Funding: This research received no external funding.

Data Availability Statement: Original contributions presented in this study are included in the article. Further inquiries can be directed to the corresponding authors.

Conflicts of Interest: The authors declare no conflict of interest.

References

1. Mirshekari, G.R.; Daee, S.; Bonabi, S.F.; Tavakoli, M.R.; Shafyei, A.; Safaei, M. Effect of interlayers on the microstructure and wear resistance of Stellite 6 coatings deposited on AISI 420 stainless steel by GTAW technique. *Surf. Interfaces* **2017**, *9*, 79–92. [CrossRef]
2. Mahmoudi, B.; Torkamany, M.J.; Aghdam, A.R.S.R.; Sabbaghzade, J. Laser surface hardening of AISI 420 stainless steel treated by pulsed Nd: YAG laser. *Mater. Des.* **2010**, *31*, 2553–2560. [CrossRef]
3. Zhang, Z.; Yu, T.; Kovacevic, R. Erosion and corrosion resistance of laser cladded AISI 420 stainless steel reinforced with VC. *Appl. Surf. Sci.* **2017**, *410*, 225–240. [CrossRef]
4. Kumara, A.S.; Durai, A.R.; Sornakumar, T. The effect of tool wear on tool life of alumina-based ceramic cutting tools while machining hardened martensitic steels. *J. Mater. Process. Technol.* **2006**, *173*, 151–156. [CrossRef]
5. Duraiselvam, M.; Galun, R.; Wesling, V.; Mordike, B.L.; Reiter, R.; Oligmüller, J. Cavitation erosion resistance of AISI 420 martensitic stainless steel laser-clad with nickel aluminide intermetallic composites and matrix composites with TiC reinforcement. *Surf. Coat. Technol.* **2006**, *201*, 1289–1295. [CrossRef]
6. Dodds, S.; Jones, A.H.; Cater, S. Tribological enhancement of AISI 420 martensitic stainless steel through friction-stir processing. *Wear* **2013**, *302*, 863–877. [CrossRef]
7. Sun, S.D.; Fabijanic, D.; Barr, C.; Liu, Q.; Walker, K.; Matthews, N.; Orchowski, N.; Easton, M.; Brandt, M. In-situ quench and tempering for microstructure control and enhanced mechanical properties of laser cladded AISI 420 stainless steel powder on 300M steel substrates. *Surf. Coat. Technol.* **2018**, *333*, 210–219. [CrossRef]
8. Nath, S.D.; Irrinki, H.; Gupta, G.; Kearns, M.; Gulsoy, O.; Atre, S. Microstructure-property relationships of 420 stainless steel fabricated by laser-powder bed fusion. *Powder Technol.* **2019**, *343*, 738–746. [CrossRef]
9. Zhao, W.; Huang, S.-J.; Wu, Y.-J.; Kang, C.-W. Particle Size and Particle Percentage Effect of AZ61/SiCp Magnesium Matrix Micro- and Nano-Composites on Their Mechanical Properties Due to Extrusion and Subsequent Annealing. *Metals* **2017**, *7*, 293. [CrossRef]
10. Akhtar, F. Microstructure evolution and wear properties of in situ synthesized TiB_2 and TiC reinforced steel matrix composites. *J. Alloys Compd.* **2008**, *459*, 491–497. [CrossRef]
11. Akhtar, F. Ceramic reinforced high modulus steel composites: Processing, microstructure and properties. *Can. Metall. Q.* **2014**, *53*, 253–263. [CrossRef]
12. Li, B.H.; Liu, Y.; He, L.; Cao, H.; Gao, S.J.; Li, J. Fabrication of in situ TiB_2 reinforced steel matrix composite by vacuum induction melting and its microstructure and tensile properties. *Int. J. Cast Met. Res.* **2010**, *23*, 211–215. [CrossRef]
13. Rajan, H.B.M.; Ramabalan, S.; Dinaharan, I.; Vijay, S.J. Synthesis and characterization of in situ formed titanium diboride particulate reinforced AA7075 aluminum alloy cast composites. *Mater. Des.* **2013**, *44*, 438–445. [CrossRef]
14. Jiang, Q.C.; Ma, B.X.; Wang, H.Y.; Wang, Y.; Dong, Y.P. Fabrication of steel matrix composites locally reinforced with in situ TiB_2–TiC particulates using self-propagating high-temperature synthesis reaction of Al–Ti–B_4C system during casting. *Compos. Part A* **2006**, *37*, 133–138. [CrossRef]
15. Tjong, S.C.; Lau, K.C. Sliding Wear of Stainless Steel Matrix Composites Reinforced with TiB_2 Particles. *Mater. Lett.* **1999**, *41*, 153–158. [CrossRef]
16. Anal, A.; Bandyopadhyay, T.K.; Das, K. Synthesis and characterization of TiB_2-reinforced iron-based composites. *J. Mater. Process. Technol.* **2006**, *172*, 70–76. [CrossRef]
17. Darabara, M.; Papadimitriou, G.D.; Bourithis, L. Synthesis of TiB_2 metal matrix composite on plain steel substrate: Microstructure and wear properties. *Mater. Sci. Technol.* **2007**, *23*, 839–846. [CrossRef]

18. Liu, Y.; Tang, M.; Hu, Q.; Zhang, Y.; Zhang, L. Densification behavior, microstructural evolution, and mechanical properties of TiC/AISI420 stainless steel composites fabricated by selective laser melting. *Mater. Des.* **2020**, *187*, 108381. [CrossRef]
19. Das, K.; Bandyopadhyay, T.K.; Das, S. A Review on the various synthesis routes of TiC reinforced ferrous based composites. *J. Mater. Sci.* **2002**, *37*, 3881–3892. [CrossRef]
20. Kanakala, R.; Rojas-George, G.; Graeve, O.A. Unique Preparation of Hexaboride Nanocubes: A first example of boride formation by combustion synthesis. *J. Am. Ceram. Soc.* **2010**, *93*, 3136–3141. [CrossRef]
21. Sekido, N.; Ohmura, T.; Perepezkoc, J.H. Mechanical properties and Dislocation Character of YB_4 and YB_6. *Intermetallics* **2010**, *89*, 86–91. [CrossRef]
22. Sadhasivam, M.; Usmaniya, M.; Berchmans, L.J.; Sanakaranarayanan, S.R.; Kumaresh Babu, S.P.; Vijayaragavan, G. A Low Temperature Calciothermic reduction Approach for the Synthesis of LaB_6 powders. *Arch. Metall. Mater.* **2024**, *69*, 1537–1541. [CrossRef]
23. Sadhasivam, M.; Berchmans, L.J.; Meenashisundaram, G.K.; Usmaniya, U.M.; Sankaranarayanan, S.R.; Kumaresh Babu, S.P. A new approach to synthesize nano-yttrium boride particle through metallothermic reduction process. *J. Min. Metall. Sect. B Metall.* **2020**, *56*, 77–87. [CrossRef]
24. Meenashisundaram, G.K.; Seetharaman, S.; Gupta, M. Enhancing overall tensile and compressive response of pure Mg using nano-TiB_2 particulates. *Mater. Charact.* **2014**, *94*, 178–188. [CrossRef]
25. Cullity, B.D.; Smoluchowski, R.J.P.T. Elements of X-ray Diffraction. *Phys. Today* **1957**, *10*, 50. [CrossRef]
26. Arhatari, B.D.; Abbey, B. Ross filter pairs for metal artefact reduction in X-ray tomography: A case study based on imaging and segmentation of metallic implants. In Proceedings of the SPIE Nanophotonics Australasia, Melbourne, Australia, 10–13 December 2017; Volume 10456.
27. Ramkumar, K.R.; Natarajan, S. Investigations on microstructure and mechanical properties of TiO_2 Nanoparticles addition in Al 3003 alloy joints by gas tungsten arc welding. *Mater. Sci. Eng. A* **2018**, *727*, 51–60. [CrossRef]
28. Ungár, T. Microstructural parameters from X-ray diffraction peak broadening. *Scr. Mater.* **2004**, *51*, 777–781. [CrossRef]
29. Apple, C.A.; Caron, R.N.; Krauss, G. Packet microstructure in Fe-0.2 pct C martensite. *Metall. Trans.* **1974**, *5*, 593–599. [CrossRef]
30. Bauri, R.; Yadav, D.; Suhas, G. Effect of friction stir processing (FSP) on microstructure and properties of Al–TiC in situ composite. *Mater. Sci. Eng. A* **2011**, *528*, 4732–4739. [CrossRef]
31. Pazhouhanfar, Y.; Eghbali, B. Microstructural characterization and mechanical properties of TiB_2 reinforced Al6061 matrix composites produced using stir casting process. *Mater. Sci. Eng. A* **2018**, *710*, 172–180. [CrossRef]
32. Yang, L.; Gao, S.; Huang, Y.; Sun, M.; Li, Y. Effect of microstructure on tensile and fatigue properties of laser-welded DP780 and DP980 high-strength steel joints. *Mater. Sci. Eng. A* **2019**, *754*, 535–555. [CrossRef]
33. Ramkumar, K.R.; Natarajan, S. Tensile properties and strengthening effects of Al 3003 alloy weldment reinforced with TiO_2 nanoparticles. *Compos. Part B Eng.* **2019**, *175*, 107159. [CrossRef]
34. Kailas, S.V. Chapter 7: Dislocations and Strengthening Mechanisms. In *Material Science*; Indian Institute of Science: Bangalore, India, 2004.
35. Ryu, H.J.; Cha, S.I.; Hong, S.H. Generalized shear-lag model for load transfer in SiC/Al metal-matrix composites. *J. Mater. Res.* **2003**, *18*, 2851–2858. [CrossRef]
36. Kulkarni, A.J.; Krishnamurthy, K.; Deshmukh, S.P.; Mishra, R.S. Effect of particle size distribution on strength of precipitation-hardened alloys. *J. Mater. Res.* **2004**, *19*, 2765–2773. [CrossRef]
37. Mintz, B. Importance of k_y (Hall-Petch slope) in determining strength of steels. *Met. Technol.* **1984**, *11*, 265. [CrossRef]
38. Takaki, S. Review on the Hall-Petch Relation in Ferritic Steel. *Mater. Sci. Forum* **2010**, *654–656*, 11–16. [CrossRef]
39. Maruyama, K.; Sawada, K.; Koike, J.-I. Strengthening Mechanisms of Creep Resistant Tempered Martensitic Steel. *ISIJ Int.* **2001**, *41*, 641–653. [CrossRef]
40. Rosenberg, J.M.; Piehler, H.R. Calculation of the taylor factor and lattice rotations for BCC metals deforming by pencil glide. *Metall. Trans.* **1971**, *2*, 257–259. [CrossRef]
41. Bramfitt, B.L. Structure/Property Relationships in Irons and Steels. In *Metals Handbook*; ASM International: Materials Park, OH, USA, 1998; pp. 153–173.
42. Lavrentev, F.F. The type of dislocation interaction as the factor determining work hardening. *Mater. Sci. Eng.* **1980**, *46*, 191–208. [CrossRef]
43. Abe, F. New martensitic steels. In *Materials for Ultra-Supercritical and Advanced Ultra-Supercritical Power Plants*; Woodhead Publishing: Cambridge, UK, 2017; pp. 323–374.
44. Sadhasivam, M.; Mohan, N.; Sankaranarayanan, S.R.; Kumaresh Babu, S.P. Investigation on mechanical and tribological behaviour of titanium diboride reinforced martensitic stainless steel. *Mater. Res. Express* **2020**, *7*, 016545. [CrossRef]
45. Ghaffari, M.; Nemani, A.V.; Shakerin, S.; Mohammadi, M.; Nasiri, A. Grain refinement and strengthening of PH 13-8Mo martensitic stainless steel through TiC/TiB_2 inoculation during wire arc additive manufacturing. *Materialia* **2023**, *28*, 101721. [CrossRef]

46. Sadhasivam, M.; Jain, V.K.S. Enhanced mechanical and thermal properties of AISI 420/TiB_2 composites fabricated by liquid metallurgy route. *Compos. Commun.* **2021**, *23*, 100550. [CrossRef]
47. Tran, D.; Lin, C.-K.; Tung, P.-C.; Lin, C.-T.; Ho, J.-R.; Iizuka, Y.; Tsao, I.-Y.; Le, T.-L. Effects of TiN content and heat treatment on microstructural changes, mechanical strength, and corrosion resistance in selective laser melting of TiN/AISI 420 composites. *Mater. Sci. Eng. A* **2024**, *900*, 146438. [CrossRef]
48. Mo, K.; Cao, L.; Zhao, D.; Long, Y.; Zhong, J.; Zhong, J.; Bi, G. Study on the microstructure and wear resistance of laser clad martensitic stainless steel 420 with different content of TiC. *Mater. Today Commun.* **2025**, *46*, 112615. [CrossRef]
49. Liang, Z.; He, P.; Zhao, Z.; Zhong, Y.; Li, Z.; Wang, M. Surface modification of 304 stainless steel by ultrasonic strengthening grind process with $Al2O_3$-MoS_2-WC hybrid ceramic particles for wear resistance enhancement. *Surf. Coat. Technol.* **2025**, *515*, 132687. [CrossRef]
50. Saha, M. Grain boundary segregation in steels: Towards engineering the design of internal interfaces. *arXiv* **2022**, arXiv:2202.12971. [CrossRef]
51. Raabe, D.; Herbig, M.; Sandlöbes, S.; Li, Y.; Tytko, D.; Kuzmina, M.; Ponge, D.; Choi, P.-P. Grain boundary segregation engineering in metallic alloys: A pathway to the design of interfaces. *Curr. Opin. Solid State Mater. Sci.* **2014**, *18*, 253–261. [CrossRef]
52. Saha, M. New frontiers in characterising ZrB_2-$MoSi_2$ ultra-high temperature ceramics. *arXiv* **2022**, arXiv:2202.11162. [CrossRef]
53. Lo, K.H.; Shek, C.H.; Lai, J.K.L. Recent developments in stainless steels. *Mater. Sci. Eng. R Rep.* **2009**, *65*, 39–104. [CrossRef]
54. Randle, V. Twinning-related grain boundary engineering. *Acta Mater.* **2004**, *52*, 4067–4081. [CrossRef]
55. Saha, M.; Pramanik, S.; Banik, R.; Maurya, P.; Singh, S.; Raj, S.V.; Madhur, D.P.; Paul, T.R.; Mitra, R.; Mondal, M.K.; et al. An Insight Into Cyclic Oxidation behavior of ZrB_2-20 Vol.% $MoSi_2$ Based Ultrahigh Temperature Ceramic Matrix Composite. In *Modern Manufacturing Systems*; Apple Academic Press: Palm Bay, FL, USA, 2022; pp. 149–163.
56. Saha, M.; Sayantani, S.; Manab, M. *Densification and Characterization of Pressureless Sintered ZrB_2-20 vol% $MoSi_2$ Ultra High Temperature Ceramic Composites*; Transactions of Powder Metallurgy Association of India: Mumbai, India, 2022; Volume 47.
57. Telle, R.; Petzow, G. Strengthening and toughening of boride and carbide hard material composites. *Mater. Sci. Eng. A* **1988**, *105*, 97–104. [CrossRef]
58. Kennedy, A.R.; Karantzalis, A.E.; Wyatt, S.M. The microstructure and mechanical properties of TiC and TiB_2-reinforced cast metal matrix composites. *J. Mater. Sci.* **1999**, *34*, 933–940. [CrossRef]
59. Williams, D.B.; Carter, C.B. The transmission electron microscope. In *Transmission Electron Microscopy: A Textbook for Materials Science*; Springer: Boston, MA, USA, 1996; pp. 3–17.
60. Gault, B.; Saksena, A.; Sauvage, X.; Bagot, P.; Aota, L.S.; Arlt, J.; Belkacemi, L.T.; Boll, T.; Chen, Y.-S.; Daly, L.; et al. Towards establishing best practice in the analysis of hydrogen and deuterium by atom probe tomography. *Microsc. Microanal.* **2024**, *30*, 1205–1220. [CrossRef]
61. Miller, M.K. *Atom Probe Tomography: Analysis at the Atomic Level*; Springer Science & Business Media: New York, NY, USA, 2012.
62. Gault, B.; Moody, M.P.; Cairney, J.M.; Ringer, S.P. *Atom Probe Microscopy*; Springer Science & Business Media: New York, NY, USA, 2012; Volume 160.
63. Douglas, J.O.; Salehiyan, R.; Saksena, A.; Schwarz, T.M.; Gault, B.; Pedrazzini, S.; Martinez-Paneda, E.; Figiel, Ł. 3D atomistic imaging of polymer nanocomposites with Atom Probe Tomography: Experimental methodology, preliminary results and future outlook. *arXiv* **2026**, arXiv:2601.12649. [CrossRef]
64. Vidilli, A.L.; Gomes, L.F.; Oliveira, A.P.; Saha, M.; Sasaki, T.; Otani, L.B.; Okulov, I. Segregation-induced microstructural refinement in a FeMnAlC-TiB metal matrix composite by laser powder bed fusion. *Prog. Addit. Manuf.* **2025**, *10*, 8171–8178. [CrossRef]
65. Saha, M.; Mallik, M. Additive manufacturing of ceramics and cermets: Present status and future perspectives. *Sādhanā* **2021**, *46*, 162. [CrossRef]
66. Mainak, S. On the Advanced Microstructural Characterisation of Additively Manufactured Alumina-Zirconia Based Eutectic Ceramics: Overview and Outlook. *SSRN 4383389* 2023. Available online: https://ssrn.com/abstract=4383389 (accessed on 23 February 2026).